

# MedVAR: Towards Scalable and Efficient Medical Image Generation via Next-scale Autoregressive Prediction

Zhicheng He<sup>1,\*</sup>, Yunpeng Zhao<sup>1,\*</sup>, Junde Wu<sup>2,\*</sup>, Ziwei Niu<sup>1,3</sup>, Zijun Li<sup>1</sup>, Lanfen Lin<sup>3</sup>, and Yueming Jin<sup>1,†</sup>

<sup>1</sup> National University of Singapore

<sup>2</sup> University of Oxford

<sup>3</sup> Zhejiang University

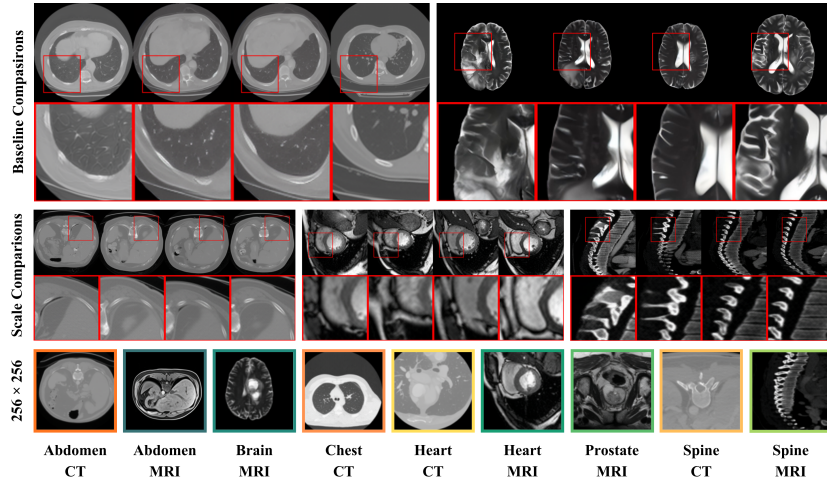


Fig. 1: **Generated samples from MedVAR.** We show baseline comparisons (top), scale comparisons (middle), and  $256 \times 256$  samples (bottom).

**Abstract.** Medical image generation is pivotal in applications like data augmentation for low-resource clinical tasks and privacy-preserving data sharing. However, developing a scalable generative backbone for medical imaging requires architectural efficiency, sufficient multi-organ data, and principled evaluation, yet current approaches leave these aspects unresolved. Therefore, we introduce MedVAR, the first autoregressive-based foundation model that adopts the next-scale prediction paradigm to enable fast and scale-up-friendly medical image synthesis. MedVAR generates images in a coarse-to-fine manner and produces structured

<sup>0</sup> \*Equal contribution. <sup>†</sup>Corresponding author.

multi-scale representations suitable for downstream use. To support hierarchical generation, we curate a harmonized dataset of around 440,000 CT and MRI images spanning six anatomical regions. Comprehensive experiments across fidelity, diversity, and scalability show that MedVAR achieves state-of-the-art generative performance and offers a promising architectural direction for future medical generative foundation models.

**Keywords:** Medical Image Generation · Visual Autoregressive Modeling · Next-Scale Prediction · Foundation model.

## 1 Introduction

Medical image generation is emerging as a cornerstone capability in modern medical AI, with the potential to support a broad range of downstream clinical and analytical tasks [28]. While foundation models in natural language and general vision have shown that a single generative backbone can generalize across diverse settings [5, 38, 24], an analogous model for medical imaging has yet to emerge. The lack of progress stems from limited understanding of three foundational factors: (i) *existing architectural principles do not provide scalability for medical image generation*, (ii) *current datasets and training paradigms predominantly focus on single-organ or single-modality settings*, and (iii) *prevailing evaluation protocols are insufficient to assess generative performance at the foundation-model level*. Addressing these questions is essential for moving beyond isolated generative methods toward a unified medical generative backbone [6, 42].

Existing architectures each offer partial advantages but also exhibit structural limitations that prevent them from developing toward this goal. GANs provide sharp images but suffer from adversarial instability and limited diversity [17, 1]. Diffusion models offer strong fidelity and robustness [20, 32], yet their iterative denoising procedures result in slow sampling unsuitable for large-scale or time-sensitive medical workflows [22]. Classical autoregressive (AR) models achieve competitive likelihoods [40], but operate on long token sequences with quadratic complexity, leading to impractical generation times for high-resolution medical data. Recent advances in Visual Autoregressive (VAR) modeling [37] suggest a transformative alternative: representing images as multi-scale token hierarchies. Crucially, VAR shifts the generation paradigm from sequential next-token prediction to parallel next-scale prediction. This formulation not only aligns with the coarse-to-fine radiological reading patterns where clinicians assess global anatomy before localized details, but also drastically reduces inference latency by generating all tokens within a scale simultaneously. By decoupling generation speed from total sequence length, VAR enables efficient, high-resolution sampling while preserving the structural consistency essential for medical imaging.

However, the effectiveness of next-scale prediction is fundamentally constrained by the scope and composition of available training data. Most public medical imaging datasets are organized around isolated anatomical regions or single modalities, resulting in organ-centric training corpora that lack unified cross-organ coverage. Such fragmentation not only restricts anatomical diversity

but also prevents models from learning globally consistent structural priors that generalize across body regions and acquisition settings. In addition, multi-site data often exhibit variable spatial scales, inconsistent cropping, and heterogeneous framing protocols [16], further complicating the learning of coherent hierarchical representations. To overcome these limitations, we curate a harmonized multi-organ dataset comprising around 440,000 CT and MRI images specifically designed to support scalable medical generation. Beyond basic quality control, we standardize spatial layouts and enforce consistent anatomical framing across organs, modalities, and acquisition sites. By unifying the global semantic scope of the data and expanding beyond region-specific collections, we enable MedVAR to learn coherent anatomical structures across diverse domains, thereby establishing the data foundation necessary for a scalable medical generative backbone.

With a suitable architecture and dataset in place, we introduce MedVAR, the first adaptation of the next-scale prediction paradigm to medical image generation. MedVAR produces anatomically consistent images via coarse-to-fine synthesis and exposes structured intermediate representations that may benefit downstream tasks. Prior evaluations largely rely on single-dataset FID-like scores without accounting for other aspects. Hence, we comprehensively evaluate MedVAR across fidelity, diversity, and scalability through extensive baseline comparisons, systematic scaling analyses, and external validation, and further introduce a designed time-aware efficiency metric that explicitly captures the trade-off between generation quality and inference cost in large-scale medical image generation [25, 9].

Overall, our contribution can be summarized as:

- We introduce MedVAR, the first next-scale autoregressive framework for medical image synthesis, enabling efficient sampling, stable scaling, and structured multi-scale representations.
- We curate a harmonized multi-organ dataset of around 440,000 CT and MRI images designed specifically to support hierarchical autoregressive generation.
- We define fidelity, diversity, and scalability as core evaluation dimensions for medical generative foundation models and provide a principled assessment framework.

## 2 Related Work

### 2.1 GAN in Medical Image Synthesis

Generative Adversarial Networks (GANs) [17] have been widely adopted for various tasks, such as MRI/CT image synthesis [29, 6], cross-modality image translation [48, 42], image reconstruction [44, 7], and super-resolution [26, 33] in medical imaging due to their ability to generate high-quality images. One of the most critical applications of GANs in medical imaging is data augmentation by generating annotated images. Several studies have employed GAN-based

approaches to synthesize lesion images for improving downstream tasks. For example, Frid-Adar et al. showed that liver lesion patches synthesized by a GAN improve CNN classification performance on CT data [14]. Similarly, Bowles et al. trained a GAN to generate synthetic brain MRI tumor images that substantially increased segmentation performance when used for data augmentation [4], and Costa et al. applied CycleGAN for retinal lesion synthesis in fundus images to improve diabetic retinopathy classification [10]. However, most GAN-based works focus on 2D medical imaging or small volumetric patches, neglecting the inherent complexity of full 3D data.

## 2.2 DM in Medical Image Synthesis

Diffusion Models (DMs) [20, 34] have recently emerged as a powerful generative paradigm, showing great potential in medical image synthesis due to their high sample quality, training stability, and flexible conditioning [32]. While recent works [22, 11] have demonstrated their effectiveness in generating 2D medical images with fine anatomical details, extending these successes to 3D remains challenging. Specifically, for 3D data, naive slice-by-slice synthesis with 2D diffusion models often leads to anatomical inconsistencies across adjacent slices. To address this, Dorjsembe et al. pioneered the volumetric approach by extending Denoising Diffusion Probabilistic Models (DDPMs) to 3D, demonstrating that direct volumetric generation significantly improves anatomical continuity compared to 2D baselines [12]. Building on this, Pinaya et al. introduced 3D Latent Diffusion Models (LDMs) to mitigate the computational burden. By compressing high-resolution medical volumes into a lower-dimensional latent space, their method enables the efficient synthesis of high-fidelity 3D brain MRI without the memory constraints typical of pixel-space diffusion [31]. Furthermore, medical foundation models such as MedDiff-FM [46] represent a step towards versatility, enabling conditional generation across multiple organs and modalities without the need for task-specific retraining.

## 2.3 AR in Medical Image Synthesis

Autoregressive (AR) models [40, 13] provide an alternative route for medical image synthesis by factorizing images into discrete tokens and generating them sequentially, enabling explicit modeling of long-range dependencies. Recent advances such as Visual Autoregressive Modeling (VAR) [37] extend this idea through next-scale prediction, producing images in a coarse-to-fine manner for improved scalability. In the medical domain, AR formulations have been applied across several tasks: AR-Seg introduces a next-scale autoregressive mechanism for multi-scale mask prediction [8]; Tudosiu et al. autoregressively synthesize high-resolution 3D brain MRI volumes using a VQVAE with a Transformer prior [39]; Luo et al. employ an autoregressive prior over latent image sequences for temporally coherent MRI reconstruction [27]; and Zhou et al. leverage token-based AR modeling with a VQ-GAN-Transformer pipeline to generate diverse

3D brain tumor regions of interest for data augmentation [47]. Beyond static synthesis, autoregressive sequence modeling of volumetric tokens has been shown to yield strong 3D priors beneficial for downstream generative and discriminative tasks [41]. Despite this progress, most AR-based medical approaches are still tailored to specific modalities, anatomical regions, or task setups, and rarely aim at a general, scalable AR framework for medical image synthesis across heterogeneous datasets. This motivates the development of MedVAR, which adapts the next-scale autoregressive paradigm to diverse medical imaging collections to achieve scalable and anatomically consistent synthesis under practical data constraints.

### 3 Data Curation

#### 3.1 Datasets

To support the development of MedVAR, we assembled a large-scale multi-modal dataset covering diverse anatomical regions and clinical imaging scenarios. The collection includes 3,146 CT volumes and 5,179 MRI volumes, spanning organs such as the abdomen, brain, chest, heart, prostate, and spine, as shown in Figure 2. Despite this broad coverage, the modality distribution remains inherently imbalanced: similar to the general trend in the community, publicly available resources are dominated by CT, while MRI data are comparatively limited in scale, acquisition diversity, and cross-center variability. To strengthen the representation of MRI, we incorporated a substantial in-house multi-center abdominal cohort consisting of 3,200 examinations, which forms a major component of the MRI data in our collection. This inclusion not only improves modality balance but also enhances the representativeness of real-world clinical environments.

**Publicly-available Datasets:** The publicly available portion of MedVAR spans a broad spectrum of anatomical regions, pathologies, and acquisition environments. These data are aggregated from widely adopted benchmarks, including Abdomen CT-1K, AMOS, BTCV, CHAOS, COVID19, KiTS2023, LiTS2017, MMWHS, MSD, SegTHOR, Spine, WORD, VerSe2019, ACDC, ATLAS, BraTS, Cardic, KiPA, and Multi-center Prostate, among others, spanning abdominal, thoracic, neurological, cardiac, and prostate imaging domains. The substantial variability across imaging protocols, resolutions, scanner characteristics, and clinical focuses establishes a highly heterogeneous training environment. This diversity forms the core public foundation of MedVAR and is essential for learning generalizable representations that transfer across anatomies and downstream medical imaging tasks.

**In-house Datasets:** To further strengthen MRI coverage beyond what is available in public resources, we include an in-house multi-center abdominal cohort consisting of 3,200 examinations collected from seven medical institutions between 2012 and 2022. The scans were acquired on systems from major vendors including GE, Siemens, and Philips, at both 1.5T and 3.0T field strengths. Each examination contains routine clinical sequences such as T2-weighted imaging, diffusion-weighted imaging ( $b=1000$ ), arterial phase, and portal venous phase,

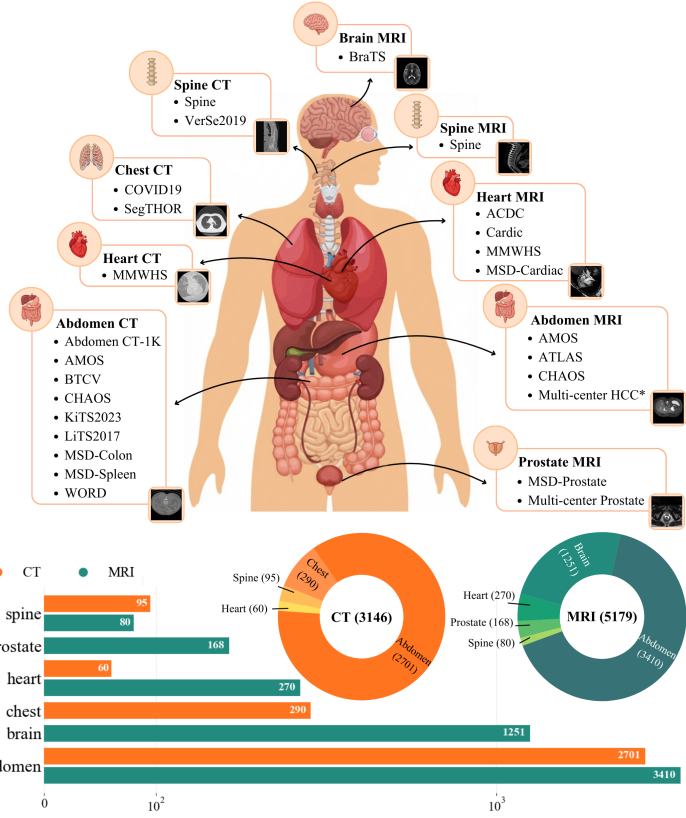


Fig. 2: **Summary of datasets used**, including voxel counts and anatomical region-modality. \* indicates in-house dataset. Voxel statistics: **CT: 3146**, **MRI: 5179**.

with many studies additionally providing dynamic contrast-enhanced acquisitions. The variation across centers, scanners, protocols, and patient populations introduces realistic clinical heterogeneity that is difficult to capture through public benchmarks alone.

### 3.2 Data Processing Framework

To mitigate domain discrepancies between CT and MRI modalities while preserving anatomical integrity, we design a unified data processing pipeline comprising geometric standardization and modality-specific intensity normalization.

*Geometric Standardization and Input Formulation.* First, we apply morphological filtering to eliminate acquisition artifacts; specifically, spurious background

regions are removed via connected-component analysis performed in both 3D volumetric and 2D slice spaces. To focus the model on relevant anatomical structures, volumes are cropped along the axial dimension to strictly retain slices containing foreground annotations. The model processes data on a slice-wise basis, treating 2D axial slices as the fundamental units for training and inference. To handle varying spatial dimensions across datasets, each slice is resized to a canonical resolution of  $256 \times 256$ . During this process, we utilize nearest-neighbor interpolation for segmentation masks to prevent label distortion, while preserving the original voxel spacing metadata to avoid introducing resampling artifacts during 3D reconstruction.

*Modality-Specific Intensity Normalization.* Given the fundamental difference in physical principles between CT (Hounsfield Units) and MRI (relative signal intensities), we adopt distinct normalization strategies. For **CT data**, pixel intensities are adjusted using a fixed window level and width to highlight soft tissue contrast. For **MRI data**, we employ a robust percentile-based clipping strategy, truncating the lowest and highest 0.5% of non-zero intensities to mitigate the impact of outliers. Following these modality-specific adjustments, all images are mapped to an 8-bit dynamic range and subsequently normalized to the interval  $[0, 1]$  prior to network input. In the end, we curated up to 438,905 images for training and testing, which serve as a substantial and diverse foundation for scalable medical image generation.

## 4 Method

### 4.1 Background: Next-scale Visual Autoregression

Next-scale visual autoregression reformulates image generation as a hierarchical prediction problem rather than a token-rasterized process. As illustrated in the original formulation [37], an image  $x$  is first encoded by a multi-scale VQVAE, which decomposes  $x$  into a sequence of discrete token maps  $\{z^{(1)}, z^{(2)}, \dots, z^{(L)}\}$ , ordered from coarse to fine spatial resolution. Each level represents either a down-sampled latent feature map or a residual refinement between two consecutive scales. Instead of modeling the joint distribution over all tokens simultaneously, VAR factorizes the generative process as

$$p(x) = \prod_{\ell=1}^L p(z^{(\ell)} \mid z^{(<\ell)}), \quad (1)$$

where a Transformer predicts the tokens of the next finer scale conditioned on all previously generated scales.

This hierarchical decomposition brings two advantages. First, sampling is significantly accelerated because each scale contains substantially fewer tokens than a full-resolution raster, and autoregression operates at the scale level rather than across spatial positions. Second, the coarse-to-fine ordering provides a natural

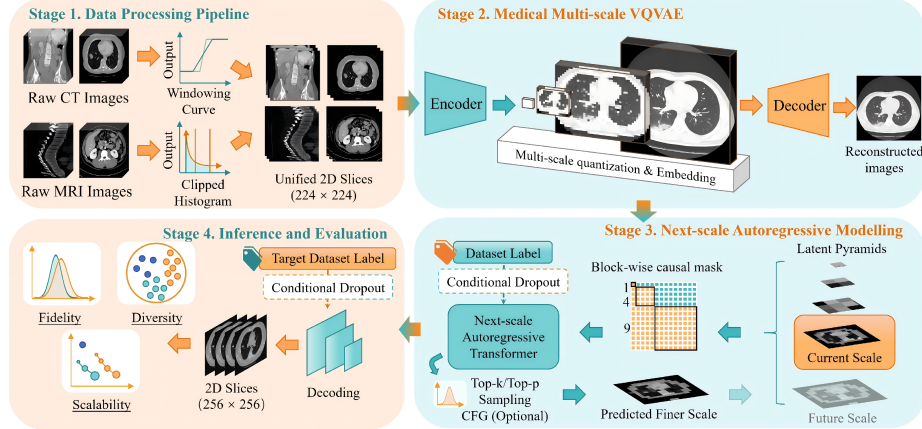


Fig. 3: **Overview of the MedVAR framework.** Raw CT/MRI data are first normalized and converted into unified 2D slices. A multi-scale VQVAE encodes images into hierarchical latent tokens, on which MedVAR performs next-scale autoregressive prediction with optional conditional dropout and CFG. During inference, multi-scale tokens are generated autoregressively and decoded to synthesize full-resolution medical images, which are evaluated in terms of fidelity, diversity, and scalability.

curriculum for modeling global structure before local detail, improving stability and scalability. In practice, the VAR pipeline consists of: (1) a multi-scale VQ-VAE that produces hierarchical discrete representations; (2) a next-scale Transformer that autoregressively predicts token maps; and (3) a decoder that reconstructs an image from all generated scales. When trained on ImageNet, this framework achieves efficient sampling and competitive fidelity with a single forward pass per scale.

#### 4.2 Overview and Problem Setting

Medical image generation poses distinct challenges compared to natural-image synthesis, as medical images exhibit strong structural regularities and systematic distribution shifts across datasets. Formally, we consider a collection of medical datasets  $\{\mathcal{D}_k\}_{k=1}^K$ , each associated with a distinct data distribution  $p_k(x)$ . The overall medical image distribution can be viewed as a mixture

$$p_{\text{med}}(x) = \sum_{k=1}^K \pi_k p_k(x), \quad (2)$$

where  $k$  indexes datasets rather than semantic classes. Our goal is to learn a scalable generative model that can synthesize anatomically coherent images across datasets while maintaining efficient sampling at high resolution.

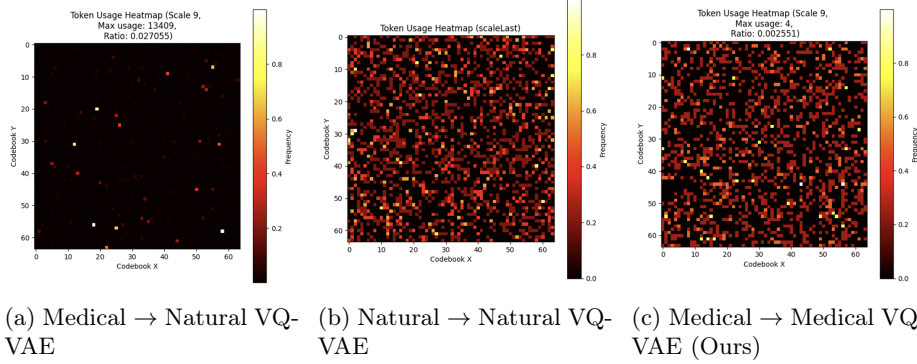


Fig. 4: **Comparison of VQVAE codebook usage heatmaps.** (a) Feeding medical images into an ImageNet-pretrained VQVAE results in extremely sparse activation (codebook collapse). (b) Natural images effectively utilize the ImageNet-pretrained codebook. (c) Our domain-specific Medical VQVAE restores dense and effective codebook utilization, capturing rich anatomical features.

To this end, MedVAR combines a medical-specific multi-scale VQVAE with a conditioned next-scale autoregressive model, as illustrated in Figure 3.

#### 4.3 Medical VQVAE for Hierarchical Discrete Representation

Effective next-scale autoregressive modeling critically depends on a discrete latent space that explicitly captures image structure across multiple spatial scales. Although the original VAR framework adopts an ImageNet-pretrained multi-scale VQVAE, directly transferring this component to medical images is non-trivial due to substantial domain differences in intensity statistics and anatomical structures.

To investigate the feasibility of direct transfer, we visualized the codebook activation patterns in Figure 4. Following prior practice (e.g., Marigold [23]), we replicated single-channel medical slices to three channels for input. As shown in Figure 4(a), when medical images are encoded by an ImageNet-pretrained VQVAE, the codebook utilization is extremely sparse, with only a negligible fraction of vectors being activated. This stands in sharp contrast to the dense and uniform activation observed when the same model processes natural images (Figure 4(b)). This *codebook collapse* phenomenon indicates a severe mismatch between the semantic features learned from natural scenes and the texture-rich, grayscale patterns of medical imaging, which consequently limits the representational capacity of the discrete tokens.

Motivated by these observations, we train a domain-specific multi-scale VQVAE from scratch on medical data. As demonstrated in Figure 4(c), our medical VQVAE successfully restores high codebook utilization, learning a rich vocabulary adapted to medical intensity distributions. The architecture largely follows

the VAR design but is optimized for medical contexts. Training employs a composite objective including pixel-wise reconstruction losses, vector quantization commitment loss, and perceptual LPIPS loss. We quantify codebook usage by counting the empirical frequency of selected code indices over a held-out set and visualizing the normalized histogram as a heatmap. The resulting medical-specific latent hierarchies provide stable and expressive discrete token sequences for subsequent autoregressive training.

The encoding and reconstruction procedures of the medical multi-scale VQ-VAE are summarized in Algorithm 1 and Algorithm 2, respectively. Here,  $\mathcal{Q}(\cdot)$  denotes the vector quantization operator that maps continuous features to discrete code indices,  $\mathcal{Z}(\cdot)$  is the codebook lookup that transforms indices into embedding vectors,  $\phi_k(\cdot)$  represents the scale-specific refinement decoder at scale  $k$ , and  $\mathcal{I}_k(\cdot)$  denotes a scale-alignment operator that resizes feature maps to resolution  $(h_k, w_k)$ .

---

**Algorithm 1: Medical Multi-scale VQVAE Encoding**


---

**Require:** Medical image  $x$ , scales  $\{(h_k, w_k)\}_{k=1}^K$   
**Ensure:** Multi-scale tokens  $\mathcal{R}$

- 1:  $\hat{f} \leftarrow \mathcal{E}(x)$ ,  $\mathcal{R} \leftarrow []$
- 2: **for**  $k = 1$  to  $K$  **do**
- 3:    $r_k \leftarrow \mathcal{Q}(\mathcal{I}_k(\hat{f}))$
- 4:    $\mathcal{R} \leftarrow \text{Push}(\mathcal{R}, r_k)$
- 5:    $\hat{f} \leftarrow \hat{f} - \phi_k(\mathcal{I}_k(\mathcal{Z}(r_k)))$
- 6: **end for**
- 7: **return**  $\mathcal{R}$

---

**Algorithm 2: Medical Multi-scale VQVAE Reconstruction**


---

**Require:** Multi-scale tokens  $\mathcal{R}$ , scales  $\{(h_k, w_k)\}_{k=1}^K$   
**Ensure:** Reconstructed image  $\hat{x}$

- 1:  $\hat{f} \leftarrow 0$
- 2: **for**  $k = 1$  to  $K$  **do**
- 3:    $r_k \leftarrow \text{Pop}(\mathcal{R})$
- 4:    $\hat{f} \leftarrow \hat{f} + \phi_k(\mathcal{I}_k(\mathcal{Z}(r_k)))$
- 5: **end for**
- 6:  $\hat{x} \leftarrow \mathcal{D}(\hat{f})$
- 7: **return**  $\hat{x}$

#### 4.4 Conditioned Next-scale Autoregressive Modeling

Given the hierarchical discrete representation, MedVAR models image generation as a next-scale autoregressive process:

$$p(x | c) = \prod_{k=1}^K p(r_k | r_{<k}, c), \quad (3)$$

where  $r_k$  denotes the discrete token map at scale  $k$ ,  $r_{<k}$  represents all coarser-scale tokens, and  $c$  is the dataset identifier, enforcing a coarse-to-fine generation order across spatial scales.

To capture anatomy-dependent domain characteristics without relying on class-based semantic labels, MedVAR conditions the autoregressive Transformer on dataset identifiers. Conditional dropout is applied during training to prevent shortcut learning and enable classifier-free guidance at inference time. The Transformer operates over scale-wise token grids with progressively increasing resolutions and is trained using standard stabilization techniques, including mixed-precision training and gradient clipping.

At inference time, discrete tokens are sampled autoregressively from coarse to fine scales and decoded through the frozen medical VQVAE. Sampling supports classifier-free guidance as well as top- $k$  and top- $p$  truncation to control the fidelity–diversity trade-off. The complete conditioned next-scale autoregressive generation process is detailed in Algorithm 3. Here,  $\text{Embed}(\cdot)$  denotes the Transformer input embedding function that maps previously generated tokens  $\mathcal{R}$  into scale-aware token embeddings while injecting the dataset identifier  $c$  via a learnable conditioning embedding.

---

**Algorithm 3: Conditioned Next-scale Autoregressive Generation (MedVAR)**


---

**Require:** Dataset label  $c$  (optional), number of scales  $K$   
**Ensure:** Generated medical image  $\hat{x}$

```

1:  $\mathcal{R} \leftarrow []$ 
2: for  $k = 1$  to  $K$  do
3:    $\mathbf{h}_k \leftarrow \text{Embed}(\mathcal{R}, c)$ 
4:    $r_k \sim \text{Sample}(\text{CFG}(p_\theta(\cdot \mid \mathbf{h}_k)))$ 
5:    $\mathcal{R} \leftarrow \text{Push}(\mathcal{R}, r_k)$ 
6: end for
7:  $\hat{x} \leftarrow \text{VQVAE\_Decode}(\mathcal{R})$ 
8: return  $\hat{x}$ 
```

## 5 Experimental Setup

### 5.1 Implementation Details

**Medical multi-scale tokenizer.** MedVAR relies on a residual multi-scale vector-quantized autoencoder to convert each image  $x$  into a hierarchy of discrete token maps  $\{r_k\}_{k=1}^K$ . The encoder downsamples by a factor of 16 and produces a latent feature map; each scale then quantizes an aligned latent using a *shared* codebook to obtain  $r_k \in \{1, \dots, V\}^{n_k \times n_k}$ , and the corresponding quantized embedding is decoded into a refinement that is subtracted from the running residual (Alg. 1). For  $256 \times 256$  inputs, we use  $K = 10$  scales with  $(n_1, \dots, n_{10}) = (1, 2, 3, 4, 5, 6, 8, 10, 13, 16)$ , yielding a total sequence length  $\sum_k n_k^2 = 680$  tokens per image. Unless otherwise stated, the codebook size is  $V = 4096$  and the code embedding dimension is  $C_{\text{vae}} = 32$ . The tokenizer is trained from scratch on the curated multi-organ medical corpus using the loss function mentioned in Sec.4.3. After convergence, the tokenizer is frozen and reused for all transformer training and sampling.

**MedVAR transformer.** Our architectural choices follow the VAR recipe [37]. The transformer is a decoder-only stack equipped with AdaLN for conditioning. Since our data are organized by datasets rather than semantic classes, MedVAR conditions on a *dataset identifier*  $c$ ; its embedding is used as the conditioning vector for AdaLN and (optionally) as a prefix token. To enable classifier-free guidance (CFG), we apply conditional dropout during training by randomly

replacing  $c$  with a null condition. We further stabilize attention by  $\ell_2$ -normalizing queries/keys before computing dot products.

**Optimization.** All transformers are trained to minimize the summed cross-entropy over token predictions across scales. We use AdamW with  $(\beta_1, \beta_2) = (0.9, 0.95)$  and weight decay 0.05. The learning rate follows a warmup + cosine decay schedule; we linearly scale the peak learning rate with the global batch size. Training is performed with mixed precision and gradient clipping for stability. Unless specified otherwise, experiments are run on 8×NVIDIA H200 GPUs.

## 5.2 Evaluation Metrics

For comparison with prior generative work, we include the standard Fréchet Inception Distance (FID) [19], and its radiology-adapted variant RadFID [43]. Additionally, we compute the Kernel Inception Distance (KID), a maximum mean discrepancy estimator that avoids Gaussian assumptions [2], and the CLIP-based Maximum Mean Discrepancy (CMMID), which measures similarity using high-level semantic embeddings [21]. Collectively, these metrics offer complementary insights into both perceptual alignment and medical-domain consistency.

To jointly evaluate generation quality and inference efficiency, we introduce a composite efficiency metric that explicitly balances fidelity and computational cost. Specifically, the efficiency score is defined as

$$\text{Efficiency} = Q \cdot (\log(1 + P))^\gamma, \quad (4)$$

where  $Q$  denotes the Fréchet Inception Distance (FID), serving as a proxy for generation quality, and  $P$  represents the inference time measured under identical hardware, batch-size, and implementation settings. Since lower FID indicates better image quality and shorter inference time implies higher efficiency, a lower efficiency score corresponds to a more favorable quality–efficiency trade-off. The logarithmic transformation on  $P$  compresses the dynamic range of inference time, preventing excessively large runtime differences from dominating the metric while still preserving relative efficiency gaps across models.

The exponent  $\gamma$  controls the relative weighting between quality and efficiency. In our experiments, we set  $\gamma = 0.1$ , which empirically balances the contributions of quality and inference time across different model families. This choice enables a fair comparison between step-dependent diffusion models and step-invariant generative approaches, such as GANs and MedVAR. In particular, the proposed formulation penalizes excessive inference cost incurred by large sampling steps in diffusion models, while avoiding overemphasizing marginal speed gains achieved at the expense of degraded image quality.

## 6 Empirical Results

### 6.1 Quantitative Comparison

Table 1 reports a quantitative comparison between MedVAR and representative GAN- and diffusion-based generative models in terms of sampling efficiency and

Table 1: **Quantitative Comparison with GAN and Diffusion-based models.** Metrics include FID, RadFID, KID, and CMMD, all of which are the lower the better. "Para.": The parameter amount of each model. The best and second-best performances are marked in **bold** and underline.

Type	Model(Step)	Time	Para.	Efficiency	FID	RadFID	KID	CMMD
GAN	StyleGAN-3	<b>0.01s</b>	54M	59.33	102.27	0.69	0.081	2.512
Diff.	DDPM-S(10)	0.17s	330M	35.83	46.84	0.06	0.032	1.035
	DDPM-S(20)	0.31s	330M	21.72	26.90	0.03	0.018	0.598
	DDPM-S(30)	0.48s	330M	17.54	20.94	0.02	0.013	0.504
	DDPM-S(50)	0.78s	330M	13.27	15.24	0.02	0.009	0.459
	DDPM-S(100)	1.55s	330M	10.63	11.63	0.01	0.006	0.432
	DDPM-L(10)	0.17s	600M	30.40	39.79	0.05	0.027	0.896
	DDPM-L(20)	0.32s	600M	18.63	23.02	0.03	0.015	0.546
	DDPM-L(30)	0.48s	600M	14.84	17.70	0.02	0.011	0.477
	DDPM-L(50)	0.78s	600M	11.79	13.55	0.01	0.008	0.438
	DDPM-L(100)	1.55s	600M	9.65	10.56	<b>0.01</b>	0.006	0.418
	DiT-S(10)	0.16s	330M	68.63	90.28	0.14	0.064	2.524
	DiT-S(20)	0.29s	330M	44.37	55.30	0.08	0.037	1.271
	DiT-S(30)	0.43s	330M	33.49	40.34	0.05	0.026	0.865
	DiT-S(50)	0.71s	330M	25.26	29.23	0.03	0.018	0.656
	DiT-S(100)	1.39s	330M	18.92	20.85	0.02	0.012	0.558
	DiT-L(10)	0.27s	600M	56.85	71.30	0.10	0.050	1.905
	DiT-L(20)	0.52s	600M	33.02	39.16	0.05	0.026	0.856
	DiT-L(30)	0.76s	600M	24.41	28.09	0.03	0.018	0.610
	DiT-L(50)	1.25s	600M	17.58	19.51	0.02	0.012	0.497
	DiT-L(100)	2.43s	600M	12.63	13.44	<u>0.02</u>	0.008	0.444
VAR	MedVAR-d16	0.09s	310M	11.94	16.59	0.06	0.004	0.217
	MedVAR-d20	0.11s	600M	7.85	<u>10.70</u>	0.03	<u>0.004</u>	<b>0.199</b>
	MedVAR-d24	0.13s	1.0B	<b>7.54</b>	10.11	0.03	0.003	<u>0.203</u>
	MedVAR-d30	0.16s	2.0B	<u>7.69</u>	<b>10.11</b>	0.03	<b>0.003</b>	0.205

image quality. GAN-based methods exhibit the fastest raw sampling speed, with StyleGAN-3 achieving 0.01s inference. However, this speed comes at the cost of substantially degraded image fidelity and medical semantic consistency, as evidenced by its significantly inferior FID (102.27) and CMMD (2.512) scores.

Diffusion-based models demonstrate a clear improvement in generative quality as the number of denoising steps increases. Both DDPM and DiT variants achieve progressively lower FID and RadFID scores when sampled with more steps; for instance, DDPM-L attains its best FID of 10.56 at 100 steps. This improvement, however, is accompanied by a sharp increase in computational cost: inference time scales linearly with the sampling steps, reaching over 1.5s for DDPM-L and 2.4s for DiT-L to generate a single high-quality image, which limits their clinical applicability.

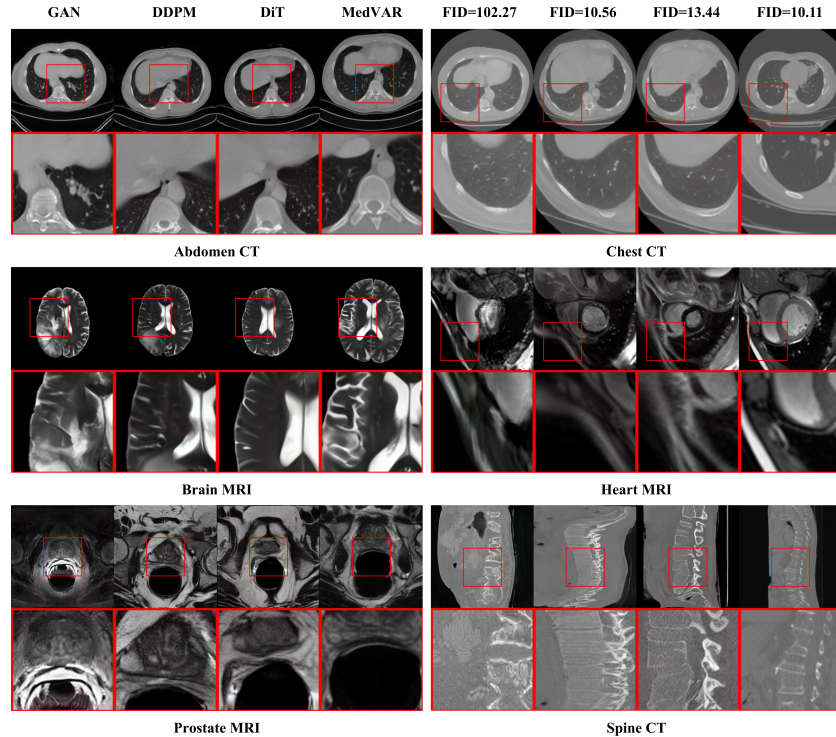


Fig. 5: **Model comparison on  $256 \times 256$  benchmark.** Each model series has been selected based on its best FID performance for comparison.

In contrast, MedVAR fundamentally changes the generation paradigm by synthesizing images through 10 coarse-to-fine autoregressive scales, rather than iterative denoising. Despite using significantly fewer generative stages compared to high-quality diffusion settings (10 scales vs. 100 steps), MedVAR achieves superior fidelity. Specifically, MedVAR-d30 delivers a lower FID of 10.11 compared to 10.56 for DDPM-L (100 steps). More importantly, MedVAR demonstrates a substantial advantage in semantic alignment metrics; it yields a CMMRD score of 0.205 and KID of 0.003, which are significantly lower than the best values achieved by diffusion baselines ( $\text{CMMRD} \approx 0.42$ ). This indicates that the hierarchical next-scale prediction allows MedVAR to capture anatomical details and radiological features more accurately. In terms of efficiency, MedVAR operates at roughly 0.1s per image (0.09s–0.16s), which is approximately 10 $\times$  to 20 $\times$  faster than diffusion models requiring extensive sampling steps. MedVAR models cluster in the optimal region of low efficiency scores (7.54–7.69), confirming that the proposed multi-scale autoregressive approach effectively breaks the trade-off between sampling speed and generation quality.

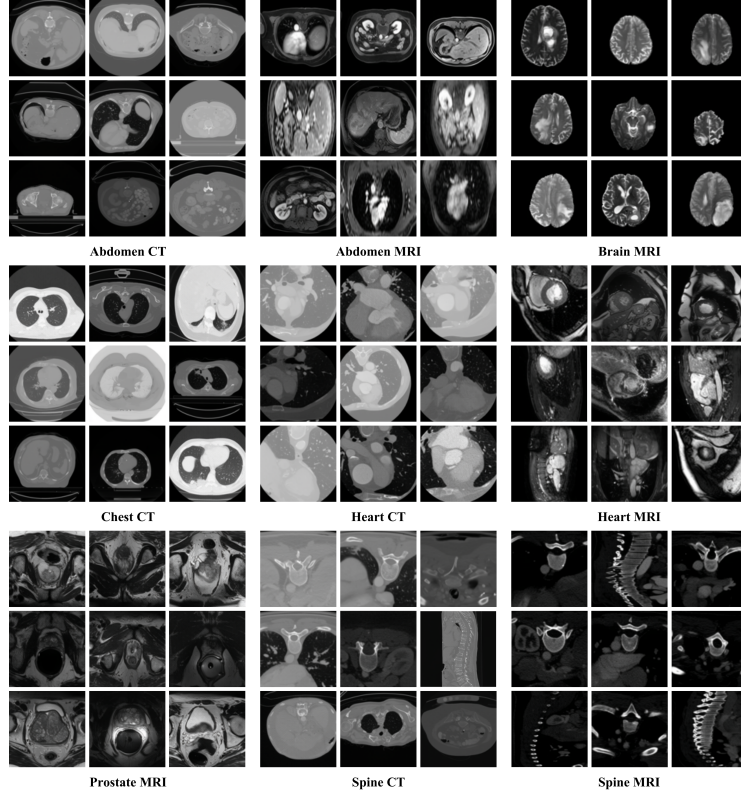


Fig. 6: **Some generated  $256 \times 256$  by MedVAR-d30.** Zoom in for a better view. From top left to right down, it shows the diverse generation results of MedVAR-d30. They are abdomen CT, abdomen MRI, brain MRI, chest CT, heart CT, heart MRI, prostate MRI, spine CT, and spine MRI results.

To visually corroborate these quantitative metrics, Figure 5 presents a qualitative comparison between MedVAR and the baseline methods. As observed, StyleGAN-3 struggles to maintain anatomically consistent geometry across modalities. In the zoomed regions, GAN outputs often exhibit non-physical shape regularization and local structural instability. For example, distorted or discontinuous bony contours in Spine CT and overly homogenized parenchymal regions in Abdomen and Chest CT, together with an evident loss of realistic high-frequency acquisition texture. Diffusion baselines (DDPM and DiT, 100-step sampling) improve global plausibility, yet their zoomed crops reveal a consistent attenuation of subtle details. In Chest CT, fine lung markings and small vascular textures are partially smoothed, and in MRI examples (Brain/Heart/Prostate), tissue interfaces appear less crisply resolved, with locally softened boundaries and reduced micro-contrast compared to the reference-like patterns expected in medical imaging.

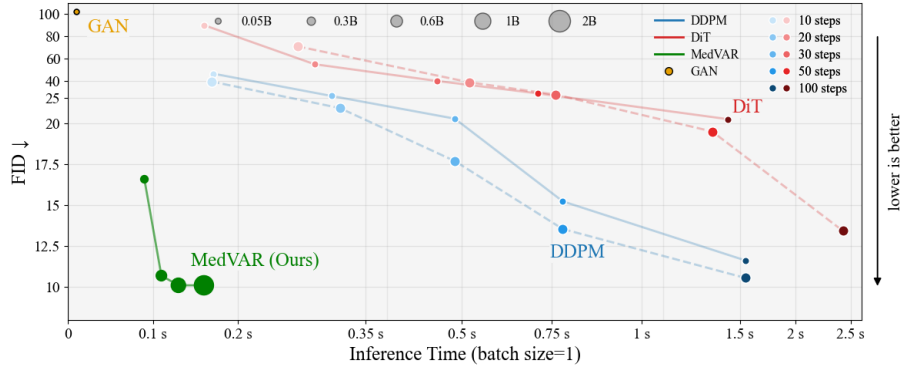


Fig. 7: **Scalability analysis of MedVAR compared with diffusion and GAN baselines.** The plot visualizes FID versus Inference Time (log scale). MedVAR achieves the best trade-off, with performance improving significantly with model size (represented by bubble area) while maintaining sub-second latency.

In comparison, MedVAR better preserves clinically coherent local structure and texture in the same ROIs. Across CT (Abdomen/Chest/Spine), it maintains sharper anatomical boundaries while retaining realistic high-frequency granularity, yielding a clearer depiction of thin cortical edges and internal textural variation. Across MRI (Brain/Heart/Prostate), MedVAR produces more stable tissue interfaces and more consistent local contrast, avoiding the structured artifacts seen in GAN outputs and the residual over-smoothing characteristic of diffusion sampling.

Beyond fidelity, a defining characteristic of a foundation model is its versatility across anatomical domains. While baseline models are typically trained and tuned for specific tasks, MedVAR utilizes a unified autoregressive backbone to master diverse distributions simultaneously. As illustrated in Figure 6, our model successfully synthesizes high-fidelity volumes across nine distinct anatomy-modality combinations, ranging from the high-contrast geometry of bony structures in CT to the subtle soft-tissue nuances in MRI, without requiring task-specific architecture modifications. This demonstrates that MedVAR has not merely memorized specific datasets but has learned a generalized representation of 3D medical anatomy.

## 6.2 Scalability Analysis

Figure 7 illustrates the trade-off between generation fidelity (FID) and inference latency across different model families and scales. The plot reveals distinct scaling behaviors: while GAN baselines achieve low latency, they suffer from mode collapse, resulting in poor FID scores ( $> 100$ ). Conversely, diffusion-based models (DDPM and DiT) exhibit a coupled cost-quality trajectory, where improving FID necessitates increasing sampling steps and inference time. As shown in the

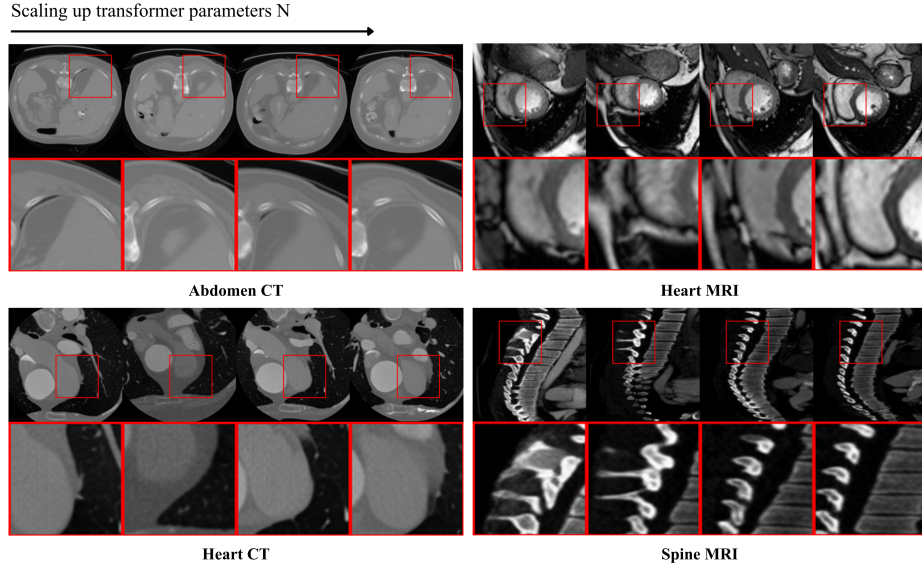


Fig. 8: **Scaling model size  $N$  improves visual fidelity and soundness.** Samples are drawn from MedVAR models of 4 different sizes.

figure, achieving an FID below 15 with diffusion models requires scaling inference time to over 1.5 seconds per image.

In sharp contrast, MedVAR occupies the optimal bottom-left region of the Pareto frontier, effectively decoupling model capacity from inference cost. The steep vertical descent of the MedVAR curve indicates that increasing the model size from 0.05B (d16) to 2B (d30) yields dramatic improvements in FID (dropping to  $\approx 10$ ) with negligible latency overhead (remaining under 0.2s). Notably, our largest 2B model achieves state-of-the-art fidelity while being approximately 10 $\times$  faster than the best-performing DDPM configuration and 15 $\times$  faster than DiT. This analysis confirms that MedVAR’s hierarchical autoregressive mechanism allows for efficient scaling, enabling high-fidelity synthesis at a fraction of the computational cost required by iterative diffusion baselines.

The impact of scaling model capacity extends beyond numerical FID scores to visible improvements in diagnostic clarity. Figure 8 illustrates the evolution of generation quality from MedVAR-d16 to MedVAR-d30. The smaller d16 model tends to produce blurred anatomical approximations, successfully capturing global layouts but failing to resolve intricate structures. As we scale to d30, we observe a distinct sharpening effect: vague tissue interfaces become crisp, and high-frequency details, such as the trabecular texture in bone structures and the distinct chambers of the heart, are faithfully reconstructed. This suggests that the next-scale prediction paradigm efficiently utilizes increased parameter counts to refine local anatomical precision rather than just memorizing global templates.

Table 2: RadFID results on different combinations of anatomies and modalities

Method	CT				MRI				
	Abdomen	Chest	Heart	Spine	Abdomen	Brain	Heart	Prostate	Spine
HA-GAN[36]	—	0.60	—	—	—	0.45	—	—	—
3D-WDM[15]	—	0.92	—	—	—	0.39	—	—	—
MOTFM[45]	—	—	—	—	—	0.43	—	—	—
MAISI[18]	0.35	—	—	—	0.46	—	—	—	—
FLUX-1[3]	0.30	0.51	0.51	0.48	0.38	0.45	0.35	0.48	0.75
SD 3.5[35]	0.32	0.45	0.47	0.48	0.35	0.43	0.37	0.58	0.77
PRX[30]	0.39	0.64	0.67	0.61	0.41	0.50	0.43	0.59	0.82
MedVAR-d30	0.05	0.08	0.46	0.07	0.11	0.19	0.25	0.16	0.14

Table 3: KID results on different combinations of anatomies and modalities

Method	CT				MRI				
	Abdomen	Chest	Heart	Spine	Abdomen	Brain	Heart	Prostate	Spine
HA-GAN[36]	—	0.114	—	—	—	0.155	—	—	—
3D-WDM[15]	—	0.227	—	—	—	0.138	—	—	—
MOTFM[45]	—	—	—	—	—	0.139	—	—	—
MAISI[18]	0.109	—	—	—	0.154	—	—	—	—
FLUX-1[3]	0.119	0.169	0.317	0.257	0.106	0.144	0.161	0.185	0.267
SD 3.5[35]	0.110	0.146	0.269	0.250	0.107	0.141	0.145	0.236	0.241
PRX[30]	0.127	0.192	0.323	0.259	0.112	0.160	0.168	0.229	0.274
MedVAR-d30	0.005	0.012	0.078	0.013	0.011	0.018	0.027	0.019	0.016

### 6.3 External Validation

To provide a comprehensive evaluation across diverse anatomical regions and imaging modalities, we compare MedVAR with a broad range of generative models on the same validation datasets. In this setting, we prioritize **RadFID** and **KID** as primary performance indicators: RadFID offers a domain-aware assessment of anatomical fidelity that is sensitive to radiological structures, while KID serves as a robust estimator of distribution discrepancy that avoids Gaussian assumptions and remains stable under varying sample sizes.

As summarized in Tables 2 and 3, these metrics reveal that MedVAR significantly outperforms both medical-specific baselines like HA-GAN and large-scale text-to-image models including Stable Diffusion and other similar methods. Notably, MedVAR achieves substantial improvements in distribution metrics. For example, while strong baselines such as SD 3.5 record KID scores in the range of 0.10–0.25, MedVAR consistently reduces KID to below 0.03 in most anatomies, with improvements approaching an order of magnitude in several cases. Similarly, MedVAR substantially reduces RadFID across most anatomies and modalities, lowering values from the 0.30–0.80 range observed in baseline methods to below 0.20 in the majority of cases. It is important to acknowledge that this evaluation

Table 4: Ablation study on inference-time sampling and guidance strategies for MedVAR. All results are reported with a fixed random seed (seed=42).  $\Delta$  denotes the FID change relative to the baseline configuration (lower is better).

Description	Para.	Model	CFG	Top- $p$	Top- $k$	FID $\downarrow$	$\Delta$
Baseline	310M	MedVAR-d16	$\times$	$\times$	$\times$	18.21	0.00
+ Top- $k$	310M	MedVAR-d16	$\times$	$\times$	0.95	17.83	-0.38
+ Top- $p$	310M	MedVAR-d16	$\times$	900	0.95	17.23	-0.98
+ CFG	310M	MedVAR-d16	4	900	0.95	16.59	-1.62
+ Scale up	2.0B	MedVAR-d30	4	900	0.95	10.11	-6.66

setting inherently introduces biases related to FOV and orientation mismatches between generated samples and reference sets. However, the fact that MedVAR maintains such low distance metrics despite these challenging mismatches suggests that the model has successfully captured intrinsic 3D anatomical priors rather than merely memorizing training views.

## 7 Ablation Studies

We conduct an ablation study on MedVAR-d16 to examine the effect of common sampling and guidance strategies, including classifier-free guidance (CFG), top- $k$  truncation, and top- $p$  (nucleus) sampling. All experiments are performed with a fixed random seed and identical model weights to isolate the impact of inference-time configurations. Table 4 reports FID, together with  $\Delta$ , defined as the FID change relative to the baseline setting without CFG or truncation.

Enabling top- $k$  alone yields a modest improvement over baseline ( $\Delta = -0.38$ ), indicating that truncation helps suppress low-probability token sampling. Adding top- $p$  on top of top- $k$  further improves fidelity ( $\Delta = -0.98$ ), suggesting complementary benefits from nucleus sampling. Finally, enabling CFG provides the largest additional gain and achieves the best overall FID (16.59,  $\Delta = -1.62$ ), demonstrating that guidance and truncation jointly contribute to improved medical image synthesis quality.

## 8 Conclusion

MedVAR presents a next-scale autoregressive framework that improves both scalability and anatomical consistency for medical image generation. By coupling a medical-domain multi-scale VQ-VAE with conditioned next-scale prediction, the model learns a unified generative backbone across heterogeneous CT and MRI cohorts while maintaining a coarse-to-fine synthesis process. This formulation enables fast sampling with strong preservation of global structure and fine-grained radiological details, offering a practical alternative to step-heavy diffusion models and instability-prone GAN variants. Extensive experiments on

diverse public and multi-center datasets demonstrate competitive fidelity and robust cross-domain behavior. Moreover, MedVAR scales favorably with model capacity, achieving high-quality generation with sub-second ( $\approx 0.1\text{--}0.2$  s) latency per image under practical settings. Looking forward, the framework provides a natural foundation for incorporating richer conditioning signals, including organ and lesion attributes, text prompts, or segmentation priors, to support controllable and clinically meaningful generative workflows.

## References

1. Arjovsky, M., Chintala, S., Bottou, L.: Wasserstein generative adversarial networks. In: Precup, D., Teh, Y.W. (eds.) *Proceedings of the 34th International Conference on Machine Learning. Proceedings of Machine Learning Research*, vol. 70, pp. 214–223. PMLR (2017), <https://proceedings.mlr.press/v70/arjovsky17a.html>
2. Binkowski, M., Sutherland, D.J., Arbel, M., Gretton, A.: Demystifying mmd gans. In: *International Conference on Learning Representations* (2018)
3. Black Forest Labs: Flux.1-dev. <https://huggingface.co/black-forest-labs/FLUX.1-dev> (2025), huggingface model repository
4. Bowles, C., Gunn, R., Hammers, A., et al.: Gan augmentation: Augmenting training data using generative adversarial networks. *arXiv preprint arXiv:1810.10863* (2018)
5. Brown, T., Mann, B., Ryder, N., Subbiah, M., Kaplan, J.D., Dhariwal, P., Neelakantan, A., Shyam, P., Sastry, G., Askell, A., et al.: Language models are few-shot learners. *Advances in neural information processing systems* **33**, 1877–1901 (2020)
6. Chartsias, A., Joyce, T., Dharmakumar, R., Tsafaris, S.A.: Adversarial image synthesis for unpaired multi-modal cardiac data. In: *Simulation and Synthesis in Medical Imaging. Lecture Notes in Computer Science*, vol. 10557, pp. 3–13. Springer (2017)
7. Chen, C., et al.: Semantic-aware generative adversarial nets for unsupervised domain adaptation in medical imaging. *IEEE TIP* (2018)
8. Chen, T., Wang, C., Chen, Z., Shan, H.: Autoregressive medical image segmentation via next-scale mask prediction. In: *International Conference on Medical Image Computing and Computer-Assisted Intervention*. pp. 24–34. Springer (2025)
9. Child, R.: Very deep vaes generalize autoregressive models and can outperform them on images. *arXiv preprint arXiv:2011.10650* (2020)
10. Costa, P., Galdran, A., Meyer, M.I., Niemeijer, M., Abrâmoff, M., Mendonça, A.M., Campilho, A.: End-to-end adversarial retinal image synthesis. *IEEE transactions on medical imaging* **37**(3), 781–791 (2017)
11. Croitoru, F.A., Hondu, V., Ionescu, R.T., Shah, M.: Diffusion models in vision: A survey. *IEEE transactions on pattern analysis and machine intelligence* **45**(9), 10850–10869 (2023)
12. Dorjsembe, Z., Paoletti, T., Frayne, R., MacDonald, M.E.: Three-dimensional medical image synthesis with denoising diffusion probabilistic models. In: *Medical Imaging with Deep Learning* (2022), <https://openreview.net/forum?id=Oz7lKWVh45H>
13. Esser, P., et al.: Taming transformers for high-resolution image synthesis. In: *CVPR* (2021)

14. Frid-Adar, M., Diamant, I., Klang, E., Amitai, M., Goldberger, J., Greenspan, H.: Gan-based synthetic medical image augmentation for increased cnn performance in liver lesion classification. *Neurocomputing* **321**, 321–331 (2018)
15. Friedrich, P., Wolleb, J., Bieder, F., Durrer, A., Cattin, P.C.: Wdm: 3d wavelet diffusion models for high-resolution medical image synthesis. In: MICCAI Workshop on Deep Generative Models. pp. 11–21. Springer (2024)
16. Glockner, B., Robinson, R., Castro, D.C., Dou, Q., Konukoglu, E.: Machine learning with multi-site imaging data: An empirical study on the impact of scanner effects. *arXiv preprint arXiv:1910.04597* (2019)
17. Goodfellow, I., Pouget-Abadie, J., Mirza, M., Xu, B., Warde-Farley, D., Ozair, S., Courville, A., Bengio, Y.: Generative adversarial nets. In: *Advances in Neural Information Processing Systems*. vol. 27 (2014)
18. Guo, P., Zhao, C., Yang, D., Xu, Z., Nath, V., Tang, Y., Simon, B., Belue, M., Harmon, S., Turkbey, B., et al.: Maisi: Medical ai for synthetic imaging. In: *2025 IEEE/CVF Winter Conference on Applications of Computer Vision (WACV)*. pp. 4430–4441. IEEE (2025)
19. Heusel, M., Ramsauer, H., Unterthiner, T., Nessler, B., Hochreiter, S.: Gans trained by a two time-scale update rule converge to a local nash equilibrium. In: *Advances in Neural Information Processing Systems* (2017)
20. Ho, J., et al.: Denoising diffusion probabilistic models. In: *NeurIPS* (2020)
21. Jayasumana, S., Ramalingam, S., Veit, A., Glasner, D., Chakrabarti, A., Kumar, S.: Rethinking fid: Towards a better evaluation metric for image generation (2024), <https://arxiv.org/abs/2401.09603>
22. Kazerouni, A., Aghdam, E.K., Heidari, M., Azad, R., Fayyaz, M., Hacihamoglu, I., Merhof, D.: Diffusion models in medical imaging: A comprehensive survey. *Medical image analysis* **88**, 102846 (2023)
23. Ke, B., Obukhov, A., Huang, S., Metzger, N., Daudt, R.C., Schindler, K.: Repurposing diffusion-based image generators for monocular depth estimation. In: *Proceedings of the IEEE/CVF conference on computer vision and pattern recognition*. pp. 9492–9502 (2024)
24. Kirillov, A., et al.: Segment anything. *ICCV* (2023)
25. Kynkäänniemi, T., et al.: Improved precision and recall metric for assessing generative models. In: *NeurIPS* (2019)
26. Ledig, C., et al.: Photo-realistic single image super-resolution using a generative adversarial network. In: *CVPR* (2017)
27. Luo, G., Huang, S., Uecker, M.: Autoregressive image diffusion: Generation of image sequence and application in MRI. *arXiv preprint arXiv:2405.14327* (2024)
28. Moor, M., Banerjee, O., Abad, Z.S.H., Krumholz, H.M., Leskovec, J., Topol, E.J., Rajpurkar, P.: Foundation models for generalist medical artificial intelligence. *Nature* **616**(7956), 259–265 (2023). <https://doi.org/10.1038/s41586-023-05881-4>
29. Nie, D., Trullo, R., Lian, J., Petitjean, C., Ruan, S., Wang, Q., Shen, D.: Medical image synthesis with context-aware generative adversarial networks. In: *International conference on medical image computing and computer-assisted intervention*. pp. 417–425. Springer (2017)
30. Photoroom: Prx-1024-t2i-beta. <https://huggingface.co/Photoroom/prx-1024-t2i-beta> (2025), huggingface model repository.
31. Pinaya, W.H., Tudosi, P.D., Dafflon, J., Da Costa, P.F., Fernandez, V., Nachev, P., Ourselin, S., Cardoso, M.J.: Brain imaging generation with latent diffusion models. In: MICCAI Workshop on Deep Generative Models. pp. 117–126. Springer (2022). [https://doi.org/10.1007/978-3-031-18576-2\\_12](https://doi.org/10.1007/978-3-031-18576-2_12)

32. Rombach, R., Blattmann, A., Lorenz, D., Esser, P., Ommer, B.: High-resolution image synthesis with latent diffusion models. In: Proceedings of the IEEE/CVF conference on computer vision and pattern recognition. pp. 10684–10695 (2022)
33. Shi, W., et al.: Real-time single image and video super-resolution using an efficient sub-pixel convolutional neural network. In: CVPR (2016)
34. Song, Y., Sohl-Dickstein, J., Kingma, D.P., Kumar, A., Ermon, S., Poole, B.: Score-based generative modeling through stochastic differential equations. In: International Conference on Learning Representations (2021), <https://openreview.net/forum?id=PxTIG12RRHS>
35. Stability AI: Stable diffusion 3.5 medium. <https://huggingface.co/stabilityai/stable-diffusion-3.5-medium> (2024), huggingface model repository.
36. Sun, L., Chen, J., Xu, Y., Gong, M., Yu, K., Batmanghelich, K.: Hierarchical amortized gan for 3d high resolution medical image synthesis. IEEE journal of biomedical and health informatics **26**(8), 3966–3975 (2022)
37. Tian, K., Jiang, Y., Yuan, Z., Peng, B., Wang, L.: Visual autoregressive modeling: Scalable image generation via next-scale prediction. Advances in neural information processing systems **37**, 84839–84865 (2024)
38. Touvron, H., et al.: Llama: Open and efficient foundation language models. arXiv:2302.13971 (2023)
39. Tudosi, P.D., Lopez Pinaya, W.H., Graham, M.S., Borges, P., Fernandez, V., Yang, D., Appleyard, J., Novati, G., Mehra, D., Vella, M., Nachev, P., Ourselin, S., Cardoso, J.: Morphology-preserving autoregressive 3d generative modelling of the brain. In: Simulation and Synthesis in Medical Imaging (SASHIMI). Lecture Notes in Computer Science, vol. 13570, pp. 66–78. Springer (2022). [https://doi.org/10.1007/978-3-031-16980-9\\_7](https://doi.org/10.1007/978-3-031-16980-9_7)
40. Van Den Oord, A., Kalchbrenner, N., Kavukcuoglu, K.: Pixel recurrent neural networks. In: International conference on machine learning. pp. 1747–1756. PMLR (2016)
41. Wang, S., Wang, C., Gao, F., Su, L., Zhang, F., Wang, Y., Yu, Y.: Autoregressive sequence modeling for 3d medical image representation. In: Proceedings of the AAAI Conference on Artificial Intelligence (2025)
42. Wolterink, J., et al.: Deep mr to ct synthesis using unpaired data. SASHIMI Workshop, MICCAI (2017)
43. Woodland, M., Castelo, A., Taie, M.A., Silva, J.A.M., Eltaher, M., Mohn, F., Shieh, A., Kundu, S., Yung, J.P., Patel, A.B., Brock, K.K.: Feature extraction for generative medical imaging evaluation: New evidence against an evolving trend (2024)
44. Yang, G., Yu, S., Dong, H., Slabaugh, G., Dragotti, P.L., Ye, X., Liu, F., Arridge, S., Keegan, J., Guo, Y., et al.: Dagan: deep de-aliasing generative adversarial networks for fast compressed sensing mri reconstruction. IEEE transactions on medical imaging **37**(6), 1310–1321 (2017)
45. Yazdani, M., Medghalchi, Y., Ashrafi, P., Hacihaliloglu, I., Shahriari, D.: Flow matching for medical image synthesis: Bridging the gap between speed and quality. In: International Conference on Medical Image Computing and Computer-Assisted Intervention. pp. 216–226. Springer (2025)
46. Yu, Y., Gu, Y., Zhang, S., Zhang, X.: Meddiff-fm: A diffusion-based foundation model for versatile medical image applications. arXiv preprint arXiv:2410.15432 (2024)
47. Zhou, M., Wagner, M.W., Tabori, U., Hawkins, C., Ertl-Wagner, B.B., Khalvati, F.: Generating 3d brain tumor regions in MRI using vector-quantization generative

adversarial networks. *Computers in Biology and Medicine* **185**, 109502 (2025). <https://doi.org/10.1016/j.compbio.2024.109502>

48. Zhu, J.Y., Park, T., Isola, P., Efros, A.A.: Unpaired image-to-image translation using cycle-consistent adversarial networks. In: *Proceedings of the IEEE International Conference on Computer Vision*. pp. 2223–2232 (2017)